Transient Flow Analysis in a Roots Blower: Experimental and Numerical Investigations

Gursharanjit SINGH[1,*], Shuaihui SUN[1,2], Ahmed KOVACEVIC[1], Qianhui LI[1], Christoph BRUECKER[1]

[1] City University of London, London, UK, EC1V0HB

[2] State Key Laboratory of Eco-hydraulics in Northwest Arid Region, Xi'an University of Technology, Xi' an, 710048, People's Republic of China

[*]Gursharanjit.Singh@city.ac.uk

Abstract. It is widely acknowledged that rotary positive displacement machines exhibit highly unsteady flow fields that affect their performance. The presence of the operational clearances impacts this unsteady flow field and further affects the performance. However, the exact nature of these unsteady flow mechanisms remains largely unknown that necessitates both detailed experimental investigations and computational modelling. Thus, the present study employs both optical visualization and unsteady Reynolds-Averaged Navier Stokes (URANS) computational modelling methods while focussing on investigating the transient flow field inside a Roots blower, a general type of the rotary positive displacement machine. Straight lobes in a Roots blower provide convenient optical access to experimentally analyse internal flow and compare it with the predictions obtained by standard computational models. In the first part of this paper, this study covers the low-speed experimental investigations using i) High-Speed Camera (HC), ii) the continuous High-Speed Particle Image Velocimetry (CPIV) and, iii) the instantaneous PIV (IPIV) obtained with a double pulse laser and a double shutter camera. Relative merits from these techniques are discussed with respect to the Roots blower unsteady flow mechanisms. In addition, computational analyses are performed using a combination of in-house and commercial modelling methods and the results are compared against the experiments. The results confirm the existence of highly three-dimensional and unsteady flow field where certain distinct flow mechanisms originating from the operational clearances impact the performance of the Roots blower. The study also highlights challenges of the experimental and computational methods used for evaluation of positive displacement machines that impact the accuracy of results.

Keywords: Positive Displacement Machines, Roots blower, Leakage Flows, PIV, CFD, Transient Flow Analysis

Abbreviations

Terms	***Symbol***
Positive Displacement Machines	*PDM*
Particle Image Velocimetry	*PIV*
High-Speed Camera	*HC*
Continuous PIV	*CPIV*
Instantaneous PIV	*IPIV*
Laser Doppler Velocimetry	*LDV*
Interrogation Area	*IA*
Turbulence Kinetic Energy	*TKE*
Unsteady Reynolds Averaged Navier Stokes	*URANS*

1 Introduction

Rotary Positive Displacement Machines (PDM) are widely used in many industrial fields. Depending on the application they may contain one or more rotating elements and a stator. Typical representatives of a single rotor machine are progressive cavity pumps and single screw compressors. Twin-rotor machines are the common type of PDM for the majority of the industrial applications. PDM can be designed with straight lobes as in Roots blowers and gear pumps, or with helical lobes as in screw compressors, expanders, and pumps. They can handle single phase fluids in the form of a gas, vapor or liquid or multi-phase fluids mixed from any combination of single-phase fluids and solids that may operate above or under atmospheric pressures. Liquid and multiphase pumps are often configured with multiple rotors. In all these machines, gaps between rotating and stationary parts have to be maintained in order to allow a safe and reliable operation but are desired to be minimal in order to reduce leakage flows, which play a critical role in the performance. The size of the gap can change due to deformations of the machine elements caused by thermal and physical loads.

Many researchers have studied leakage flows through clearance gaps in rotary positive displacement machines both experimentally and numerically. Numerical methods are mostly based either on chamber modeling [1] or computational fluid dynamics (CFD) model [2, 3]. In chamber models, it is usually assumed that the momentum change in the main domain is negligible due to the internal energy being dominant while the velocity of the leaking fluid is obtained based on the assumption of the isentropic flow through a nozzle. CFD models allow more accurate calculation of velocities both in the main and leakage paths by numerically solving governing conservation equations such as mass, energy, and momentum. The latest developments in grid generation for rotary PDMs has been described in detail by Rane et al. [4, 5]. It has led to the meshes which can be used for CFD flow calculation of the entire domain of the rotary PDMs. This grid generation method has been implemented in the commercial mesh generator SCORG allowing the use of almost all commercially available CFD solvers, ANSYS CFX 19.0 in the present case. The size of the mesh, the speed of its generation as well as the speed of calculation by commercial solvers is suitable for industrial application. However, whether these CFD-URANS based methods can sufficiently capture the internal flow field for these machines remains to be known.

Numerical procedures employing chamber models or 3D-CFD are usually validated by measurements of the integral parameters such as the total mass flow rate and power as illustrated by Kovacevic and Rane [6]. They indicated that the clearance mass flow rate can be captured well using this method. However, unless the actual leakage flow local velocities are measured, such leakage flow models cannot be fully validated. In addition, the velocity distribution in the main flow of a rotary positive displacement machine has not been studied experimentally and validation data are not available. Therefore, for the full validation of numerical calculations, it is required to obtain accurate measurements of the flow field both in the main working domain and in the clearance gaps of a rotary PDMs.

Attempts were made in the past to evaluate internal flows in screw compressors using optical methods. Sachs [7] studied the gas flows in the tip gap of a static flat rotor screw compressor. They applied the Toppler Schlieren method to obtain the swirls and shocks within the leakage gap. The influence of pressure ratio, gap shape, gap height and moving boundary on the leakage flow was investigated. This study helped in understanding leakage

mechanisms which influence mass flow rate and efficiency of these machines. Further, Laser Doppler Velocimetry (LDV) method was recommended to obtain quantitative results in the gap without interference with the leakage flow. The LDV measurements in the working chamber close to the discharge and in the discharge chamber of an oil-free compressor were reported by Gueratto *et al.* [8] while the measurement of the flow in the suction chamber of an oil-free compressor with water injection was reported by Kovacevic *et al.* [9]. However, neither of the measurements managed to give quantitative velocity values within the working domain of the compressor. These investigations were especially challenging, given screw machines with helical rotors limit optical access for the assessment of flow. An alternative to twin-lobed screw machines is a Roots blower which has straight lobes and entails similar flow characteristics.

Roots blowers usually have two straight rotors with an involute profile and two or more lobes in each. Various mechanical design studies have been performed in the past, for instance, two-lobed configurations by [14, 32-34] and three-lobed configurations by [35-37], where design methods for these machines have been documented. In practice, the presence of higher number of lobes does not make much difference in the performance except providing a stable operation and capacity for the Roots blower [38,39]. The present study employs an industrial Roots blower in a two-lobed configuration where the tip of each lobe has a step profile. This profile facilitates early closure and late opening of the suction chambers, thereby extending the compression process within the chambers. The rotors rotate in opposite directions within the casing and form a working chamber between the rotors and casing. Roots blowers do not have internal compression as the volume of the chamber remains constant while rotating. The increase of the pressure is external to the rotors due to the backflow from the high-pressure side [25-27]. Previous numerical studies have shown [40-41] that operating multi-stage Roots blowers in either series or parallel configurations can provide optimised operational performance. However, the transient flow interactions between different Roots blowers are not covered in the present study.

Recently, Liu *et al.* [10, 11] and Sun *et al*. [12, 13] established the CFD simulation model of the roots blower and validated it by measurements of mass flow rate and pressure distribution. These studies provided necessary developments previously highlighted by Voorde [42] where simplified computational models for Roots blower domain did not provide useful results indicating the need for a three-dimensional CFD models for these machines. In addition, the leakage flow in a two-lobe roots blower was predicted using a stationary mesh in CFD and the results were compared with the experimental leakage mass flow rate by Joshi et al [14]. They elaborated the Roots blower rotor profile design method and thereafter studied the impact of radial and interlobe leakages from these designs. In particular, they used a similar tip step profile similar to the one employed in the present study. Joshi et al [14] also recommended performing unsteady analysis with a deforming mesh for these machines. The advances in the single domain meshes were not possible until recently [5] while detailed optical measurements were not performed before to capture the three-dimensional flow analysis for Roots blower. Joshi et al [14] also demonstrated differences in the high pressure and low-pressure losses in performance due to the presence of the axial leakage loss highlighting their importance for the PDMs. Huang and Liu [24] conducted similar analysis using 2D numerical meshes at various rotating positions for 3 lobe twin-rotor Roots blower. They concluded the presence of large vortical flow field within the chambers which is influenced by various pressure fields and largely impacts the mixing of these vortices. Their results revealed the presence of highly transient flow mechanisms

within the 2D flow field interacting with the radial and interlobe leakage flows for the Roots blower. Similarly, several other studies [28-31, 34] have been conducted in the recent past where numerical analysis of the Roots blower was performed using both commercial and open source solvers. They indicated the presence of strong vortical flow field and mainly analysed the radial and interlobe leakages with similar conclusions in terms of the flow field. However, the understanding of these leakages using CFD methods needs to be coupled with the development of experimental techniques capable of analysing the flow domain. Thus, Sun et al [15] reported experimental developments necessary to determine velocities using optical methods which will be discussed in detail in the present study.

The flow structures arising due to the leakage flows in the working chambers can influence on the performance of a positive displacement machine in two ways: 1) Primary reduction in the performance where a leaking fluid is inherently limiting the ability of the machine to separate high pressure and low-pressure chambers. 2) Secondary mechanisms such as an increase in the turbulence, conjugate heat transfer effects, noise pulsations or cavitation processes limiting the performance of these machines. In comparison to the secondary processes, the understanding of primary processes has been well understood in the literature. However, several challenges remain that limit our understanding of the secondary flow mechanisms initiated by the leakage flows for PDMs. These may include the inability of the industrial CFD methods, lack of optical access or lack of studies where all types of leakages are combined in one study. The present study does not try to quantify all of these processes, instead, it tries to understand the general flow dynamics by performing experimental and computational studies for different leakages. It encourages future research to model all leakages together whereby the further understanding of these secondary mechanisms can be achieved.

Owing to the possibility to evaluate flow dynamics via optical access and similarity in the flow mechanisms, the study of Roots blower forms a suitable test case for validation of CFD calculations. It reveals major measurement and modeling challenges associated with fluid dynamic investigations for positive displacement machines. Any accurate CFD method must be robust enough to capture the unsteady 3D flow dynamics at their operating conditions. This paper provides experimental investigations using three different optical flow visualization techniques, namely high-speed (HC), continuous PIV (CPIV) and Instantaneous PIV (IPIV) for the given Roots blower. Afterward, the experimental investigation of flow in optical roots blower by phase-locked Particle Image Velocimetry (PIV) [15] was used to validate the CFD simulation model. The CFD computations have been prepared by applying the dynamic grids from SCORG and were solved in ANSYS CFX 19.0 flow solver to obtain the flow patterns. Finally, the simulation flow regime is compared with the experimental results and general flow dynamics are studied in detail. In particular, this paper targets to address the following research questions:

1) What are the reliable optical methods to capture the unsteady flow field for positive displacement machines?
2) What is the reliability of the state-of-art unsteady computational methods to determine the flow field inside a Roots blower?
3) Which flow mechanisms influence or determine the three-dimensional unsteady nature of the Roots blower flow field?

2 Experimental Analysis using Optical Methods

2.1 Experimental setup

Roots blower (see Figure 1) used in this investigation has twin-lobe rotor configuration mounted on parallel shafts that rotate in opposite directions with air as a working fluid. The suction and discharge pipes connect to the inlet and outlet domains respectively. The air passes through the Roots blower via the inlet port and fills into the suction chamber formed by the casing and the rotors. Three types of flow leakage gaps are recognized in the Roots blower, namely (i) tip gap between rotors and the casing, (ii) interlobe gap between the rotors, and (iii) axial gap between the side of the lobes and the enclosed casing. Some of the key geometrical dimensions have been listed in Table 1.

The optical Roots blower was mounted in the test rig that allows measurements of pressures, mass flow rates, and power while operating at the variable conditions. The optical access to the Roots blower allowed the use of the PIV laser technique for acquiring velocities inside the main and leakage flow paths. The layout of the test rig is shown in Figure 1a. The optical window was designed to allow optical access through two locations (see Figure 1c). One of the windows is positioned radially while the other is on the side of the machine. The side window is used for collecting measurements through the reflection image in the mirror (L) in Figure 1c. The equipment used for measurements was introduced in detail in the previously published paper by the authors [15]. Considerations towards the structural integrity of the Perspex glass window dictated limiting operational speed and pressure ratio to be lower than the designed parameters of the prototype (5275rpm, pressure ratio 2.6). The optical window, shown in Figure 1b, can sustain only limited temperatures achieved at low speeds and pressures. However, as shown later in this paper the operation at lower speeds does not impact the general flow dynamics and the conclusions drawn in this study.

Table 1. The main geometrical parameters of the Roots blower

Items	Specification	Items	Specification
Diameter of the rotor [mm]	101.3	Tip gap [mm]	0.1
Axis distance [mm]	63.12	Interlobe gap [mm]	0.17
Rotor length [mm]	50.5	Axial gap [mm]	0.15
Displacement volume [l/rev]	0.4618	Width of tip step [mm]	6.4

Table 2. Operating conditions for the Roots blower tests

Test Type	Inlet pressure	Inlet temperature	Outlet pressure	Outlet temperature	Pressure ratio	Speed	Mass flow rate
Units	[Pa] x 10^5	[K]	[Pa] x 10^5	[K]	[-]	[rpm]	[kg/s]
HC test	1.011	298.4	1.075	304.5	1.063	464	0.00118
CPIV test	0.986	300.1	1.048	303.1	1.063	464	0.00111
IPIV test	0.975	300.6	1.045	306.2	1.072	464	0.00103
IPIV test	0.976	299.4	1.04	302.5	1.067	625	0.00261

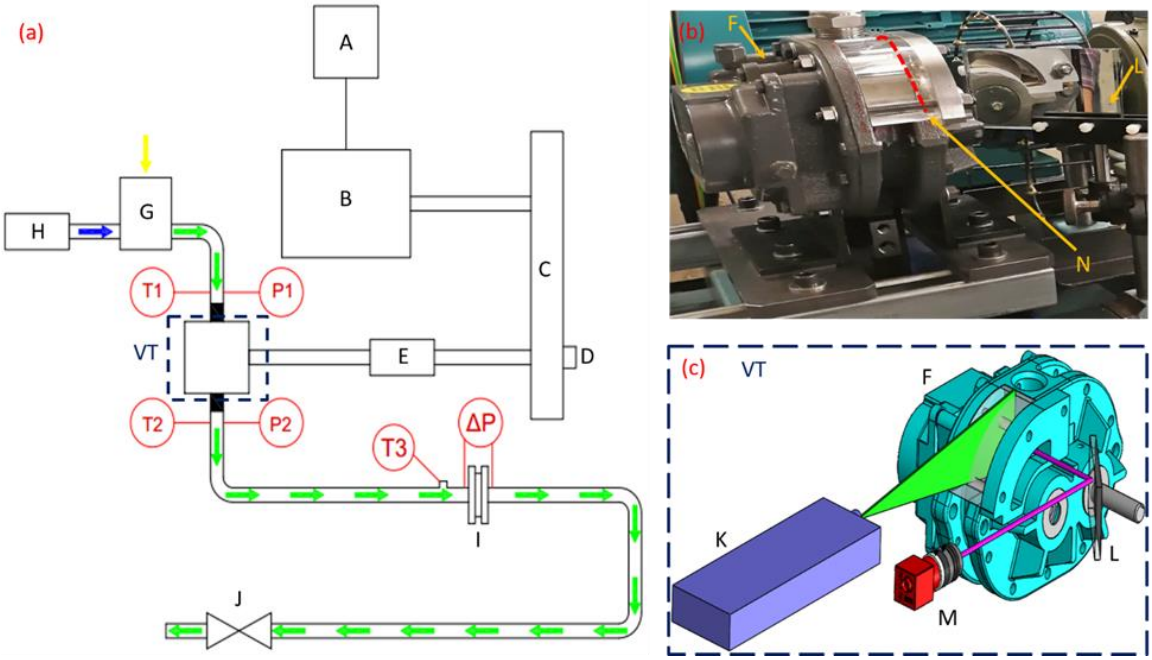

Figure 1. Roots blower test rig and diagram of visualizing test

A - inverter, B – electromotor, C- pulleys, D – shaft encoder, E- torque meter, F – roots blower, G – smoke tank, H – smoke machine, I – orifice plate, J – valve, K – Light source, L – surface mirror, M – double shutter camera, N – Position of Laser plane, T1 – suction temperature transducer, P1 – suction pressure transducer, T2 – discharge temperature transducer, P2 – discharge pressure transducer, T3 – upstream temperature transducer, ΔP – differential pressure across an orifice plate

Table 3. Set-up details the three test rigs

Method	Light source	Camera	Phase-lock
High-speed camera test (HC)	Day-light lamp (ARRI M18)	High-speed camera (Photron APX RS 25k)	no
Continuous time-resolved PIV test (CPIV)	Continuous laser (Raypower 5000)	High-speed camera (Photron APX RS 25k)	no
Instantaneous PIV test (IPIV)	Double-pulse laser (Dantec Dual power 200-15)	Double-shutter camera (Flow sensor E0)	Yes

Three optical tests were investigated in this study namely, the high-speed camera test (HC), the continuous time-resolved PIV test (CPIV) and the instantaneous PIV test (IPIV).

Table 3 and Figure 2 provides the camera, laser type and set-up details for these three methods. Each method employed a different light source, namely the day-light lamp (HC), continuous laser (CPIV), and double-pulse laser (IPIV). The day-light lamp can light the entire flow field while laser-based methods illuminate a plane within the flow field. The air intake flow was seeded with tracer particles of 2μm diameter, generated by a smoke machine (H) vaporizing a liquid glycol. The smoke tank G (see Figure 1a) was used to

distribute the smoke homogeneously. The mixture of air and smoke then enters the roots blower and passes through the working chamber. The test system consists of a synchronizer to take the recording at a fixed crank angle position i.e. instantaneous PIV measurements were performed in a “phase locked” manner. The shaft encoder shown in Figure 1a was used to synchronize laser operation, and the camera to the required position of the lobe was recorded by a Timer box.

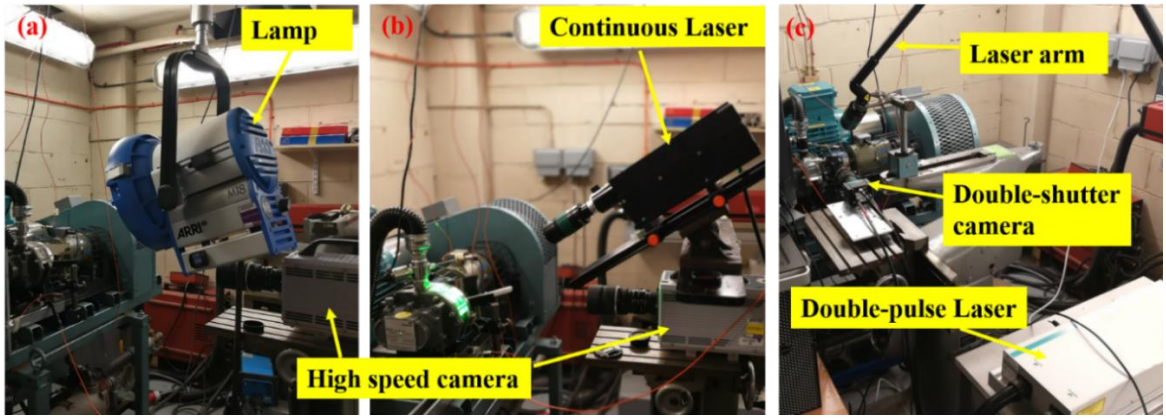

Figure 2: Optical methods applied to study Roots blower flow dynamics (a) HC test, (b) CPIV test, (c) IPIV test

During the HC and the CPIV test, a series of continuous pictures of the flow field were taken. The camera frame speed for the HC test was 10000fps with the resolution of 768*368 pixels. The recording would start after the release of the smoke into the blower. Usually, the time duration of the recording is 1 second which would be sufficient for 6 cycles of rotors at 464rpm and 625rpm speeds to be captured. During the CPIV test, the laser sheet was located 0.5cm away from the inner wall of the window inside the chamber, as shown by the dotted red line with label ‘N’ in Figure 1b. The sample rate of the camera was 10000fps, and the resolution was 512*512 pixels. A series of images were recorded for 1 second which captured 6 rotor cycles. These images were compared and the velocity vectors were calculated from cross-correlation (Raffel et al [16]) of small interrogation windows in consecutive frames of CPIV recording. The processing of the datasets for both HC and CPIV methods was performed the in-house code.

The IPIV method employed an Nd:YAG laser with maximum 200mJ at the wavelength of 532nm to illuminate the smoke particles. This laser was mounted on the laser arm and the beam was transformed to the laser sheet by using appropriate lenses at the end of the laser arm. The laser sheet plane (N) was 0.5 cm inside the chamber from the window (see Figure 1b). Once the lobe reached the required crank angle, the first laser pulse was emitted to light up the flow field enabling the camera to take the first picture at a resolution of 2048×2048 pixels. After a short interval of time of 2-50 µs, dependent on the maximum velocity in the flow field, the camera takes the second picture with a second pulse. Recorded pairs of pictures were processed to obtain the velocity field. The double-shutter images in the IPIV tests were processed by the Dynamic Studio software using the Adaptive PIV method. The Adaptive PIV method is an automatic and adaptive cross-correlation method which iteratively adjust the size and the shape of the individual interrogation areas (IA) in order to adapt to local seeding densities and flow gradient, further details of which could be found in [16]. The spacing between central positions of interrogation areas (IA) is determined by the grid step size parameter set at a value of 16 x 16 pixels. The minimum IA size was set as 32 x 32

pixels and the maximum IA size was set as 128 x 128 pixels. The desired number of seeding particles per IA was specified to be 10. No window or filter function was applied in the settings. Peak Height validation parameter was enabled to allow calculation for the ratio between the two highest correlation peaks. The value of Peak Height ratio was higher than the specified value in order to validate the calculated displacement. Minimum Peak Height ratio of 1.05 was set for the validation of the cross-correlation with a Universal Outlier Detection in a 5 x 5 pixels area, with a minimum normalization of 0.10 pixel which would correspond to the typical root-mean-squared noise level of the PIV data [17] and acceptance limit of 2.0. The presence of the Universal Outlier Detection algorithm helped to prevent outliers from disturbing the iterations and thus the velocity measurements. The validation is achieved by first applying peak validation on the image cross-correlation and secondly by comparing each vector to its neighbours using the Universal Outlier Detection algorithm.

All three tests were performed at similar operating conditions as shown in Table 2. The inlet pressure is atmospheric at the time of testing. The discharge pressure was controlled by the discharge valve to obtain a similar pressure ratio during the test. Since speed and operating pressure ratios in the test were lower than the machine design parameters, the presence of main flow rate and leakage velocity helped in the better visualizing the results, especially with HC and CPIV methods.

Currently, Roots blower consisted of two-lobed rotors that can be divided into six steps with intervals of 30°. The crank angles of shooting position were specified to be 10°, 40°, 70°, 100°, 130°, and 160°. Figure 3 shows the rotor positions at the crank angle of 10° and 70°.

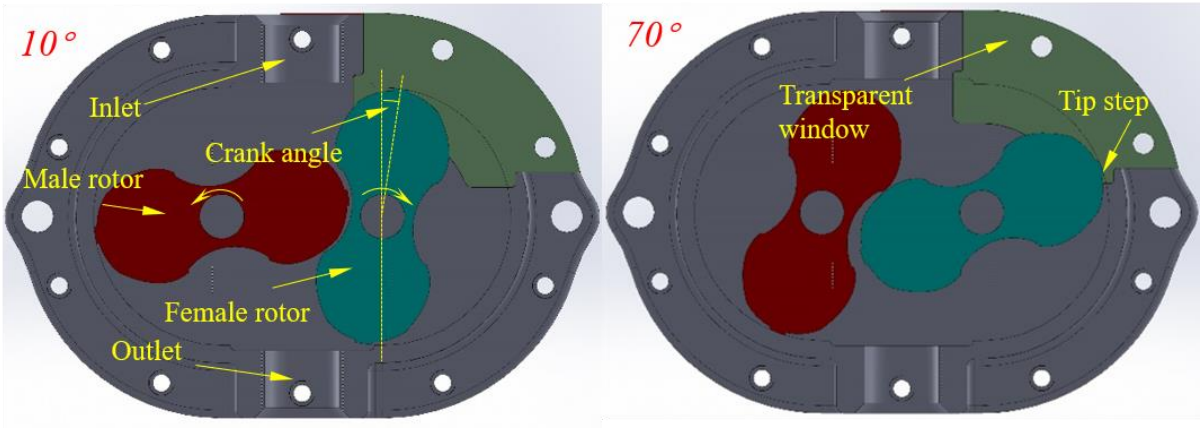

Figure 3: Rotor position at 10° and 70° degrees

2.2 Flow Visualization

Figure 4 shows a group of snapshots taken by the high-speed camera in the HC test (left) and CPIV test (right). The images for HC test are blurry and it is difficult to identify a single smoke particle in the field of view. However, the flow pattern can be visualized by the density of the smoke in each position. Playing the video from a series of images between 57° to 60° crank angle revealed the presence of a vortex at the back of the lobe as marked at the 57° position. This vortex must be arising from the combined effect of the low-pressure wake field created by the lobe and the backflow from the tip-leakage clearance, which can be identified in the video of the HC results. The structure of the vortex was found to be three-dimensional and it was visualized in the HC method because the ambient light allows for particles in different planes to be visible in the same image. However, the presence of a

large number of small-sized particles makes it difficult to both visualize and quantify the flow structures.

Figure 4 (right) shows the CPIV pictures at crank angles varying from 70° to 72°. These images are sharper than the HC images (left) and particles can be observed clearly. However, only a two-dimensional image can be captured due to the plane illumination by the sheet laser for CPIV. The fluid close to the outside wall mainly flows from right to left indicating the backflow, which is likely to be induced by the trailing from clockwise rotating lobe and the associated tip-leakage flow. The leakage flow was not visible due to the reflection from the surfaces and due to light scattering as indicated by the yellow line in the top right image in Figure 4. Furthermore, the window inside the red line was scratched which additionally prevents taking a clear image of the flow field near the outside casing wall, especially the tip-leakage flow. However, the CPIV test showed the vortex behind the lobe rotating anti-clockwise as indicated by the circle. The shape and the position of the vortex changes as the rotor rotates indicating high mixing in the flow field.

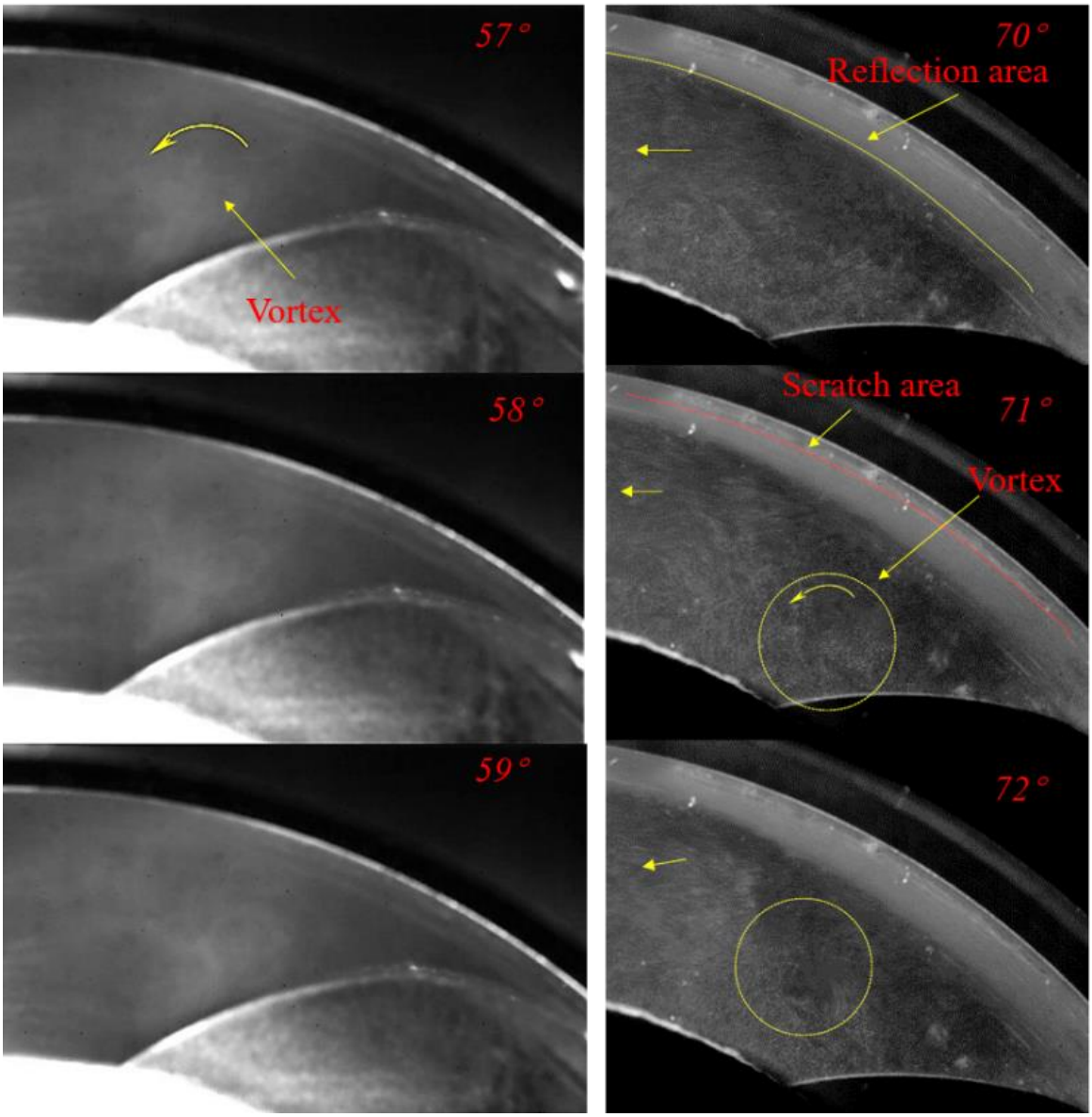

Figure 4 Unprocessed images from HC test (left) and CPIV test (right); crank angle labels are shown in red

In order to increase visibility near the casing region, the lobe, bolts and the inner surface of the chamber were painted matt-black and the scratches were polished before the IPIV tests were obtained. As shown in the unprocessed IPIV images for 10º and 70º crank angle positions in Figure 5, the scratches disappear during the IPIV test while the reflection area becomes much narrower. The tracked particles can be distinguished easily in both pictures. At the crank angle of 10°, the windows show the front of the lobe that has just closed the suction port. At the crank angle of 70°, the window shows the area behind the lobe connected to the suction chamber. Owing to the large differences in the flow field type, these two positions are selected to compare the rest of the analysis between different test methods. Two shadows are visible in the frames, one at the top left of the window and another on the right side of the window which significantly reduces the visibility of the flow.

In summary, all methods are able to provide a different level of resolution of vortices trailing behind the rotor lobes where IPIV gives the best clarity and HC gives the lowest clarity. However, the HC method carries a unique advantage in terms of small visualization of the three-dimensional flow field but does not allow clarity as to the CPIV and IPIV methods.

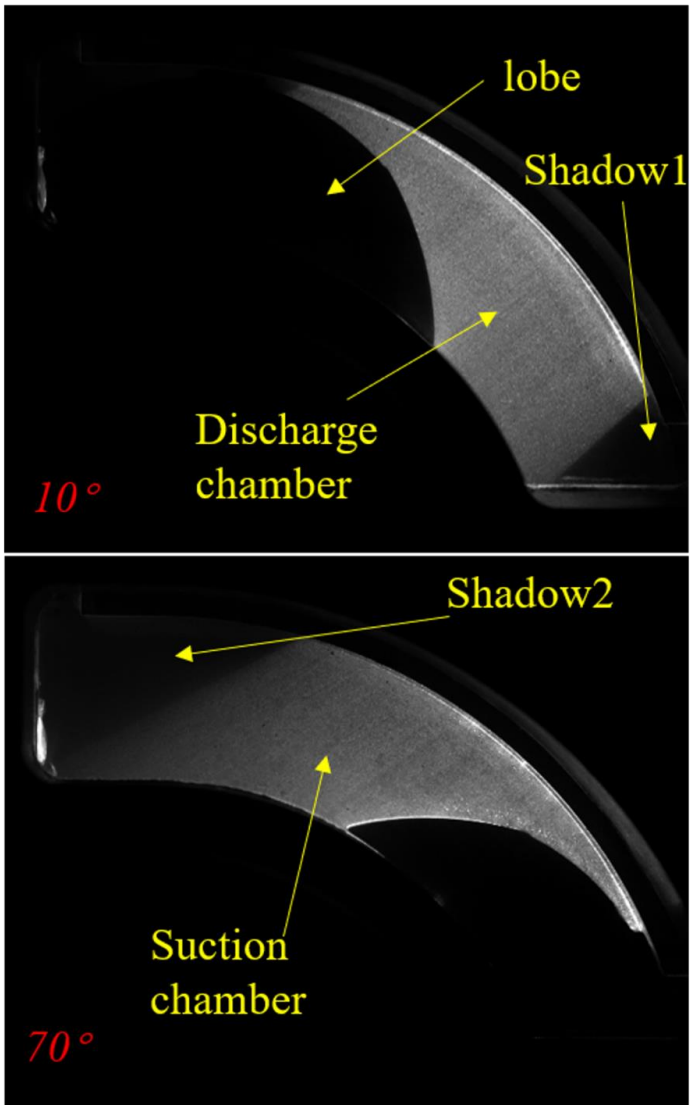

Figure 5: Unprocessed images of the tracer particles at 10º and 70º crank angle positions from IPIV test

2.3 The main chamber velocity field

The instantaneous velocity vectors at the crank angle of 10° and 70° were calculated from IPIV test. The mean velocity vectors are obtained by averaging the instantaneous velocity vectors from all 120 measured cycles. To compare with the IPIV results, the pictures at the crank angle 10° and 70° of every cycle from the HC and CPIV results were processed to obtain the instantaneous velocity vector. The HC average velocity vector was calculated by averaging 4 instantaneous velocity vector fields at the same position, and the CPIV average velocity was computed using 6 readings at the same position.

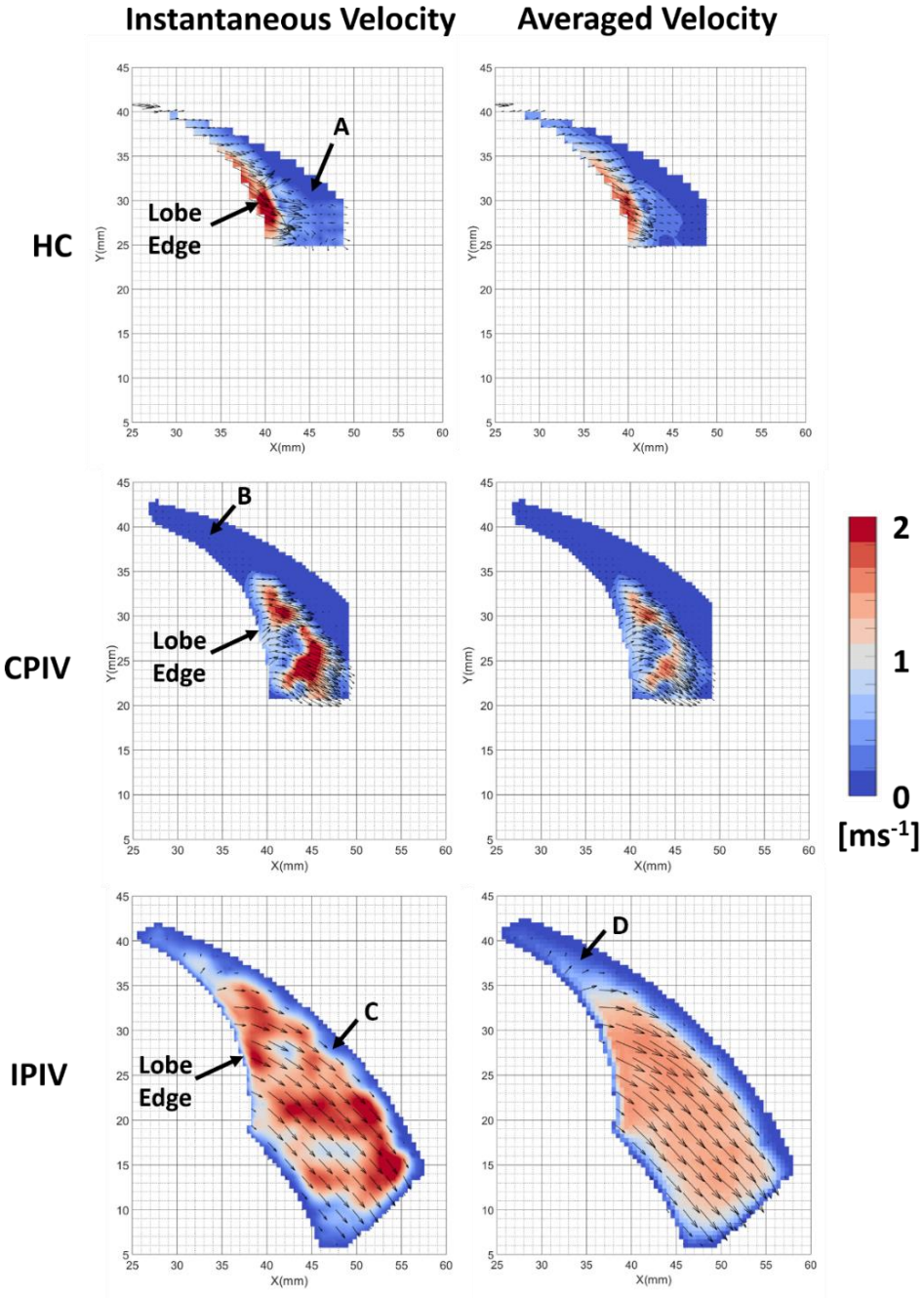

Figure 6. Instantaneous and phase-averaged velocity field at 10º crank angle

Figure 6 provides instantaneous (left) and phase-average 120 cycles (right) velocity magnitude fields superimposed with velocity vectors at the crank angle of 10°. All images

were plotted in the same coordinates system. The results from HC, CPIV, and IPIV are shown in a matrix form. The corresponding instantaneous and phase-averaged velocity vector distributions in the overlapped area of three figures show different flow patterns. IPIV test shows nearly uniform flow-field in the domain that cannot be seen in HC and CPIV test. In addition, in the area 'A' in the HC test and in area 'B' of the CPIV test, the velocity magnitudes were approximately equal to 0. For the HC test, the reason could be the inability of the image processing software to identify the movement of particles and calculate the correct speed. For the CPIV, it is most likely because of the surface reflection as shown in Figure 4. In addition to that, it was identified that the time-resolved PIV (CPIV) did not have sufficient resolution to accurately track particles and ensure that the same particles are observed in consecutive frames. In contrast, the IPIV test employed a powerful laser with the resolution of 2048*2048 allowing the full image of the polished window to be recorded. Small regions of low velocity near the casing region (see labels C and D) can be observed in the IPIV results. However, that does not impact the ability to capture the main flow accurately. Therefore, all of the particles in the full flow field were bright enough to be used to calculate their velocity vectors except in shadow in the right bottom corner, see Figure 5. IPIV velocity vector results offer the highest quality of results amongst the three methods and are most likely to show the real flow field. It should be noted that 1 pixel was removed at the walls to account for any inaccuracy in obtaining these results. However, the contour interpolation method may at times see a zero velocity at the lobe edge and correspondingly show a sudden rise in the velocity magnitude from 0 to 2 m/s on the lobe edges as seen in Figure 6. Thus, velocity magnitude at the moving wall edges may not match the moving wall (lobe) speed at in the figures for the remaining part of the paper.

Comparing the instantaneous and phase-averaged flow, the latter velocity vector distributions are not significantly different from the instantaneous values except that the maximum velocity magnitude is reduced. Because of averaging 120 instantaneous vector fields in the IPIV velocity vector distribution, the large turbulent fluctuation and instantaneous motions of the flow are removed. However, it must be noted that IPIV results exhibit large deviation in the flow velocities from cycle to cycle revealing highly unsteady nature of the flow field inside a Roots blower operating at nearly 10% of its designed speed.

Figure 7 shows the instantaneous and phase-averaged velocity magnitude field superimposed with velocity vectors at the crank angle of 70°. Note that the IPIV results at 70° employ a separate contour color limits to ensure better visibility of the flow features. In all cases, the fluid near the lobe follows in the direction of movement of the lobe at the same velocity as the lobe. CPIV and IPIV indicate both, the flow direction and the vortex are in the opposite direction of the lobe movement. However, it is not possible to ascertain that this is a back-flow induced by the tip-leakage flow as shown in Figure 4. It should be noticed that the velocity magnitude for IPIV is much higher than CPIV indicating that the time-resolved PIV does not have sufficient resolution to capture the fast-moving particles accurately. The maximum instantaneous velocity reached 10.3 m/s in the region 'C' in Figure 7 on IPIV measurement results. It is highly counterintuitive for a majority of the flow at 70° to move in the backward direction, which is in contrast to the general observation at 10° where flow moves along the lobes. It is possible that such a backflow at 70° might be arising from the three-dimensional vortices being formed within the main chambers rather than being affected by the leakage flow. We will be reviewing this postulate while examining three-dimensional flow from CFD analysis in the later sections of this paper.

Large differences between IPIV and CPIV results at both instantaneous and averaged charts could be arising from different accuracy of these methods. The frame speed of the camera in CPIV is not sufficient to capture the movement of the high-velocity smoke particles. For the IPIV test, the time interval of the two pulses of the laser is set to 15μs. It corresponds to an equivalent frame speed of about 66000 fps in CPIV. Thus, the particles in the CPIV pictures at 10 kHz frame rate cannot correlate correctly because the out-of-plane motion and image pair loss in the consecutive images is too large. Hence, the CPIV test in this paper can show the variation of vortex and flow pattern but is not suitable to calculate the velocity vector in high-speed flow regions. The power of the continuous laser, the resolution and the frame speed of the camera used in this test limit the capability of the CPIV test. In spite of these limitations, the CPIV results could show the dynamics of the flow during rotation of the lobe and the richness of vortices present in the flow which is not available with IPIV. Therefore, both quantitative measurement methods have individual advantages and disadvantages for use in such highly unsteady flows.

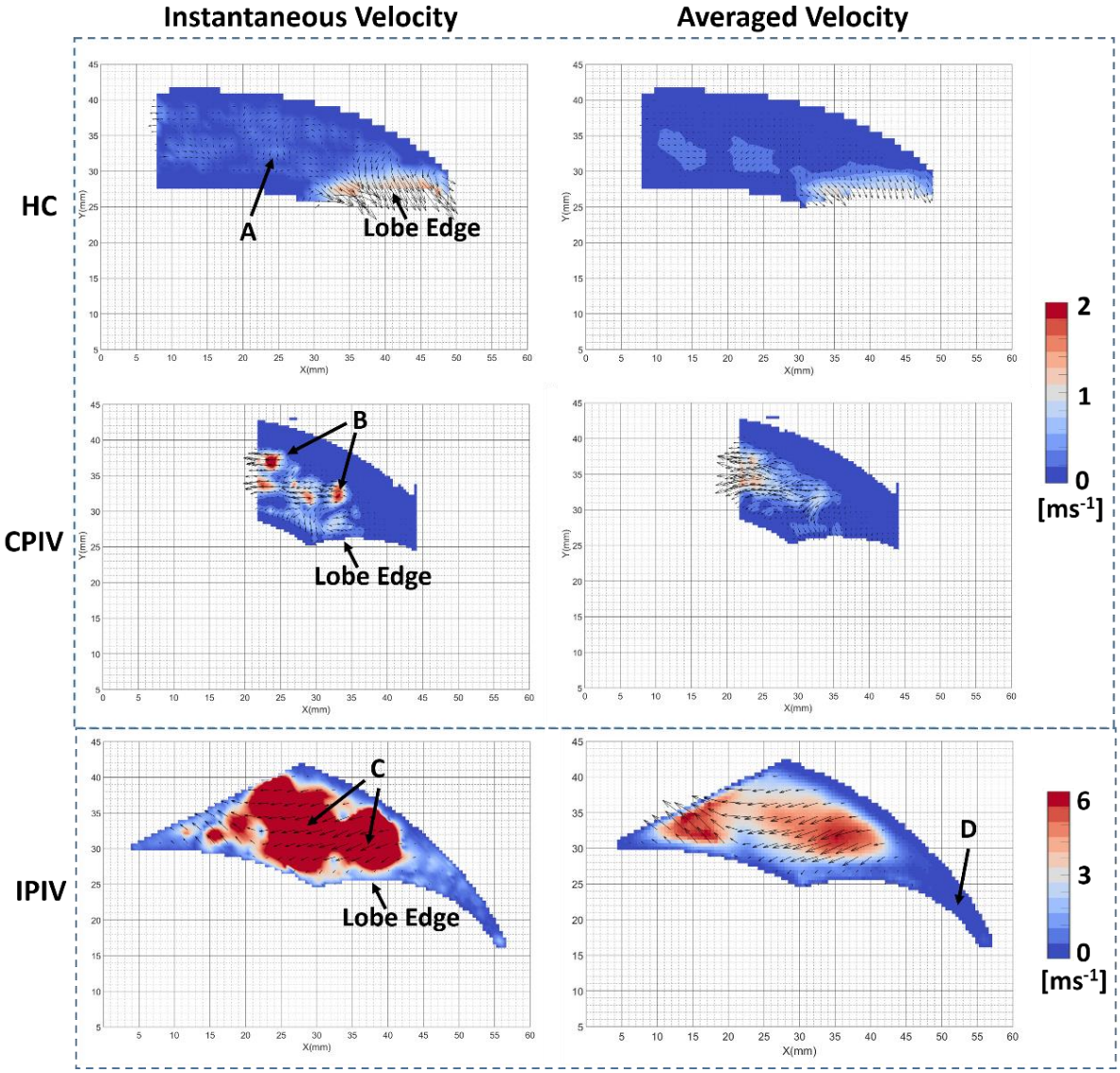

Figure 7. Unsteady and average velocity field at the crank angle of 70º

The flow in the area 'D' of IPIV is the downstream tip leakage flow which shows some very low-velocity regions. It is not clear is this because of the recirculation or the error in

measurements due to the reflection from the surface or if the radial leakage is indeed very low in this case. In order to understand this better, the next section will be looking at the gap region in detail and further compare experimental results against the numerical predictions. A higher resolution that needs microscope lens and shorter laser time interval could be used to capture the velocity vector of the leakage flow in and around the tip clearance in the future which may give additional insight into the leakage flows in the Roots blower.

2.4 Additional IPIV measurements in the gap region

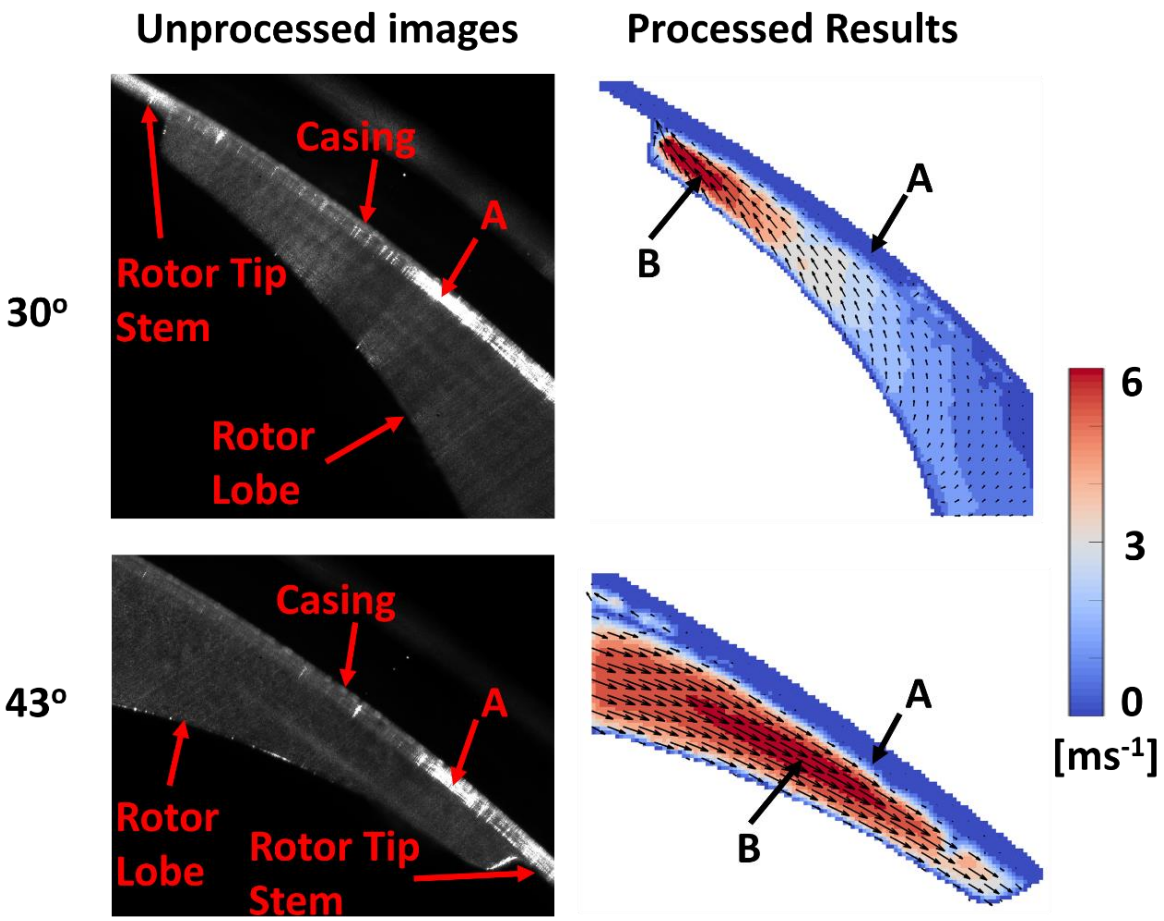

Figure 8. Rotor radial gap side IPIV measurements at 30° and 43° crank angles

Figure 8 provides unprocessed images and processed results from the rotor gap measurements obtained using IPIV method. The processed results consist of 120 measurement cycles averaged value of velocity magnitude as a contour plot superimposed with velocity vectors indicating the direction of flow at each location. The data processing was made with a scaling of 0.4mm length (tip stem height) corresponds to the 78.5 pixels. Note that the results correspond to the crank angle position of approximately 30° and 43° at 464rpm while running at a pressure ratio of 1.02. This pressure ratio is slightly different from 1.072 pressure ratio used in the previous section as reported in Table 2. The processed results (right side images) in Figure 8 show near zero velocity magnitude region (see label 'A') in the immediate vicinity of the casing arising from lack of accurate measurement due to the presence of sharp streak lines as shown in the left side column of unprocessed images. Moving away from the casing, regions of high velocities can be observed (see label 'B').

There is a tendency of the leakage flow at 30° crank angle position as female lobe are moving towards the flow in the clockwise direction. Some of the flow is expected to scrap above the gap in this region. For 43° crank angle, the effect seems to be arising from the build-up of flow field by the rapid movement of the male lobe which is rotating in the anti-clockwise direction and must be restricting bulk incoming flow from the inlet port and thereby providing a local accelerating in the flow field. This effect can be seen in the upper part of figure 11 (see 40° and 70° crank angle positions) and general flow field in the inlet port area in figure 14 (laser plane). Further, owing to the highly unsteady nature of the flow field the high fluctuations in the velocity magnitudes and directions were observed for both crank positions. The results of the gap measurements indicate that the leakage flow has high speed (~6ms^{-1}) in contrast to the previous near radial gap observations from IPIV measurements in Figure 6. Due to the insufficient data at the corresponding crank angle position, this argument remains unconfirmed but the presence of a highly three-dimensional unsteady flow field is evident. The next part of this paper discusses the numerical analysis of the flow in Roots blower, at the same conditions as in experiment and comparison between numerical and experimental results.

2.5 Cycle-to-cycle fluctuations in the flow field

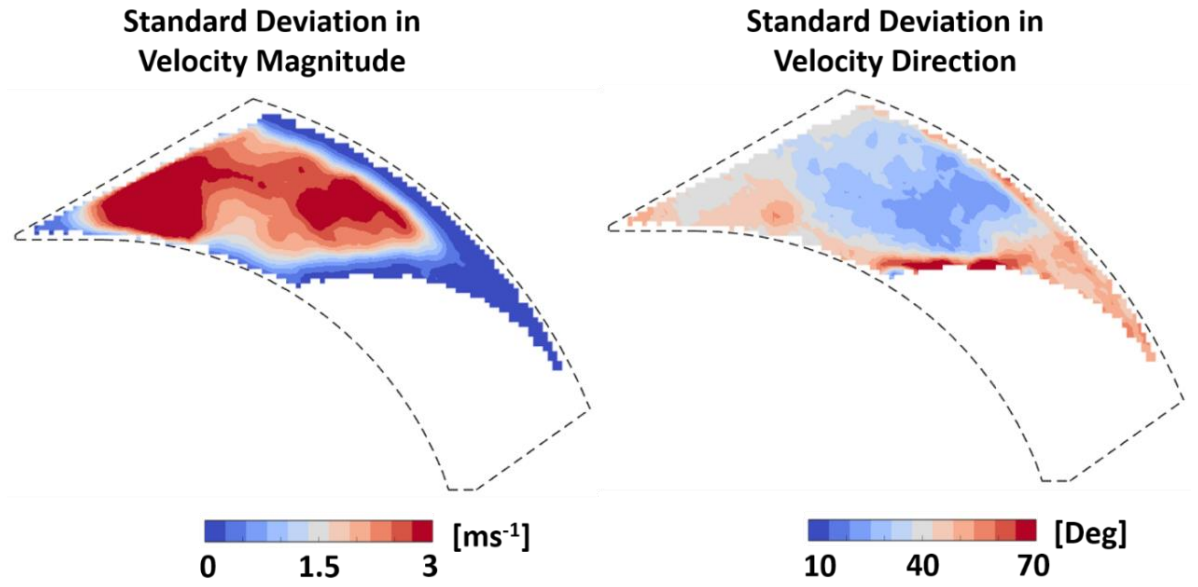

Figure 9. Cycle-to-cycle fluctuations in IPIV measurements for 120 cycles at 464rpm

Before comparing experimental and simulation results, it is worth pointing out the cycle-to-cycle fluctuations in the experiment arising due to the unsteady nature of the flow between 120 cycles. This is important since the URANS analysis computes averaged turbulence in the flow and is likely to produce different results than the experiment. The Roots blower studied in this paper was operated at nearly 10% of its design speed due to the practical limits encountered before optical measurements could be obtained. This inherently exacerbates the unsteady flow nature between different measurement cycles as demonstrated in section 2.4. In Figure 9 the standard deviation in the velocity magnitude and the velocity direction (flow angle) across 120 measurement cycles at 464rpm speed and 70° crank angle were plotted. Distinct regions of high flow speed deviations and flow angle

deviations can be observed in the plot. It is worth noting that the majority of the flow direction variation happens near the rotor lobe surface and casing walls. This could be arising from the minor fluctuations in the crank angle position between 120 measurement cycles that can quickly reverse flow direction near moving rotor surfaces. In case of velocity magnitude within the main chamber, it can be assumed that the differences in the crank angle position are marginal, especially since the variation is between 1-2^{o} against the 30^{o} difference between crank angle positions. Such fluctuations in the flow speed could arise due to the periodic harmonics in the flow field or due to the presence of completely random fluctuations at low-speed conditions.

3 Computational analysis for Roots blower

3.1 CFD Set-up

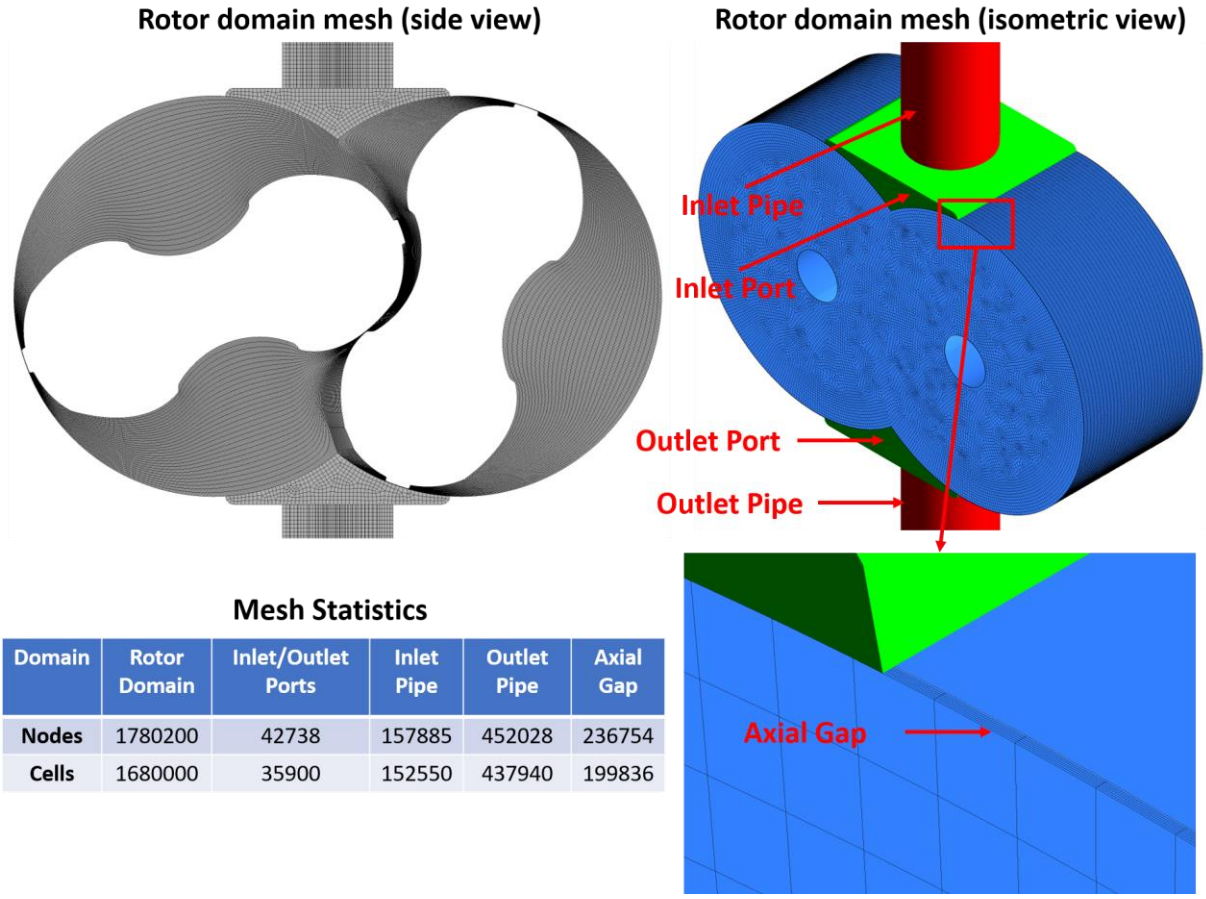

Mesh Statistics

Domain	Rotor Domain	Inlet/Outlet Ports	Inlet Pipe	Outlet Pipe	Axial Gap
Nodes	1780200	42738	157885	452028	236754
Cells	1680000	35900	152550	437940	199836

Figure 10. Domain mesh snapshots indicating deforming rotor mesh, stationary inlet, and outlet domain meshes along with axial gap mesh

A computational set-up of the Roots blower was prepared to simulate the flow field previously measured in section 2. Since details of the CFD set-up and grid independence study are already provided in the previous publication by authors [18], only a brief description of the set-up is given here. The computational set-up involved generating rotor domains and simplified ports meshes to simulate the unsteady nature of the Roots blower. This required a stationary fluid domain for inlet and outlet chambers to be extracted from a CAD model of the Roots blower. Simulation set-up of the moving rotor domain involved

generating meshes using in-house grid generation software SCORG v5.6 [4-6]. These moving rotor domains meshes are usually generated by keeping mesh stationery with respect to either casing or rotor. It provides a useful frame of reference for these meshes, based on which further shape, size, and quality of the meshes can be developed. Rane et al [4-5] have detailed these meshing strategies and recommended the usage of casing-to-rotor conformal mesh obtained using algebraic transfinite interpolation and numerical smoothing in SCORG v5.6. It also helped in preserving the shape of the small-sized tip and side steps on the lobes (Figure 3 shows rotor lobes and tip shape).

Table 4. CFD set-up for analysis of the Roots blower

Setting	Specification	Setting	Specification
Advection scheme	High-resolution	Turbulence numerics	1st order
Transient scheme	2nd order backward Euler	Wall model	No slip with adiabatic walls
Turbulence model	SST with wall functions	Iteration per timestep	20
Heat transfer model	Total energy including viscous terms	Inlet/Outlet condition	Opening with static pressure & temperature
Domain initialisation	Standard atmospheric conditions	Working fluid	Air as Ideal gas
Time step at 464 rpm	3.592E-4	Convergence criteria	RMS 1E-4

Four refined levels of rotor domain mesh were generated to achieve the grid independence study. Cycle averaged mass flow rate and chamber pressure flow field was used as a convergence criterion to determine grid independent mesh for this study. The final selected grid consisted of 180 angular positions for single interlobe rotation which means that the grid files were generated with the angle interval of 1°. The stationary grids were generated using ANSYS-Mesh consisted of inlet grids, outlet grids and axial-gap grids with six layers of grids in each axial gap. In order to provide smooth convergence of the simulation, the inlet and outlet boundary conditions were imposed at far upstream and downstream of the Roots blower. The lengths of the suction pipe and discharge pipe were set to three and nine times of the pipe diameter, respectively. This placement ensured that the Roots blower flow field is not influenced by the inlet and outlet boundary conditions. Hexahedral grids with 889405 nodes for the stationary grids i.e. inlet, outlet, and axial gap domain grids were generated for all cases. The rotor grids and the stationary grids are combined and connected via general grid interfaces available in the Ansys-CFX v19.0. Figure 10 provides snapshots of the final grid independent mesh selected for this study. Ansys-CFX v19.0 solver was used to perform unsteady RANS simulations for the Roots blower. The working fluid was set as air with ideal gas properties. The high-resolution scheme was used for the advection term while the second order backward Euler scheme was used for the unsteady term. Turbulence numerics were computed using SST (Shear Stress Turbulence) turbulence model. The Y+ value on viscous surfaces within the radial gap of lobes was kept below 2 in all cases. The time step was determined to be 3.592E-4 for the rotor speed of 464rpm. The number of computing iterations was set to 20 for each time step, allowing reasonable stability in the solution before moving to the next time step. The

static pressure was used to set the inlet and outlet opening boundaries. The pressure at the inlet and outlet boundary conditions was imposed based on the measured values corresponding to 464 and 625 rpm as detailed in Table 2. The root-mean-square residual target value was set at 1E-4 for each time step and 3 complete cycles of rotors were simulated after the required stability of the residuals, chamber pressures and mass flow were achieved. This allowed for sufficient stability in the converged solution and the last cycle values were used to report results in this paper. Table 4 summarises these settings for the various simulations.

3.2 Comparison between the experimental and simulation results

Figure 11 and Figure 12 show the velocity magnitude contours superimposed by the velocity vectors (not to scale between CFD and Experiments) for both simulation and experimental results at six rotor positions and two rotor speeds, 464 and 625 rpm respectively. The colour bars of experimental and CFD results show the velocity magnitude in the plane of the laser sheet. The experimental results are averaged from unsteady velocity vectors in 120 measured cycles. The velocity vectors were processed in the laser sheet plane. A green coloured frame superimposed on the CFD results represents the border of the visible area of the PIV pictures so that the flow field in the frame can be compared with the measured velocity field.

With the exception of 40^o and 70^o crank angles, the general flow direction is captured reasonably well by CFD while the differences in the velocity magnitude and peak regions of 'high' velocity (= $6ms^{-1}$) are consistent. In general, CFD shows higher velocity magnitude than the corresponding experimental values. One possible cause for this could be due to the low mixing of the small vortices in CFD. At 70^o crank angle, a complete mismatch in the flow direction between the CFD results and measurements was observed. Looking at all CFD figures from crank angles 10^o to 160^o, the flow in front of the lobe travels at a uniform speed along with the lobe while the flow behind the lobe trails and forms several small and large vortices. This trend is also observed for experimental results with an exception of the 70^o crank angle when it shows flow moving in the opposite direction than the lobe.

The second trend observed from this comparison is the general increase in the flow speed and turbulence as the rotor speed is increased from 464rpm to 625rpm. Finally, in the experimental results, it is not possible to see any presence of the leakage flow but a high-speed jet appears behind the lobe (see label 'B' in Figure 11) from 40^o to 100^o crank angle positions. As indicated before, the experiments were unable to capture the leakage flow near the casing region. Thus, it cannot be determined with absolute certainty, if the presence of radial leakage flow is large enough to impact the flow field within the chamber.

In the next section that follows, the source of the leakage jet 'B', which is arising from the formation of the corner vortex (see label 'CV2' in Figure 13) from axial leakage flows will be revealed and discussed.

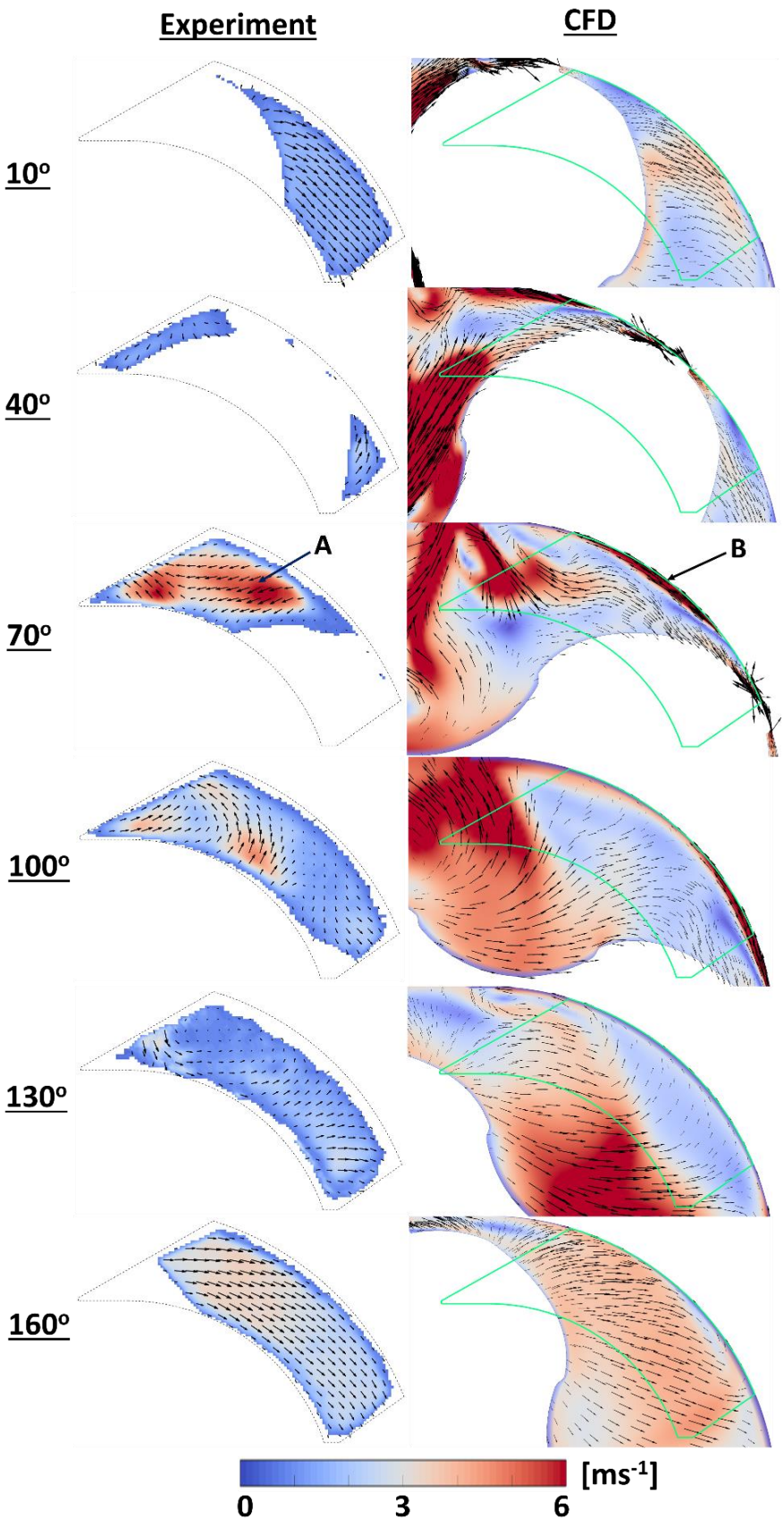

Figure 11. Comparison between the PIV results and CFD results at various crank angle positions and 464rpm rotor speed (Vectors not to scale)

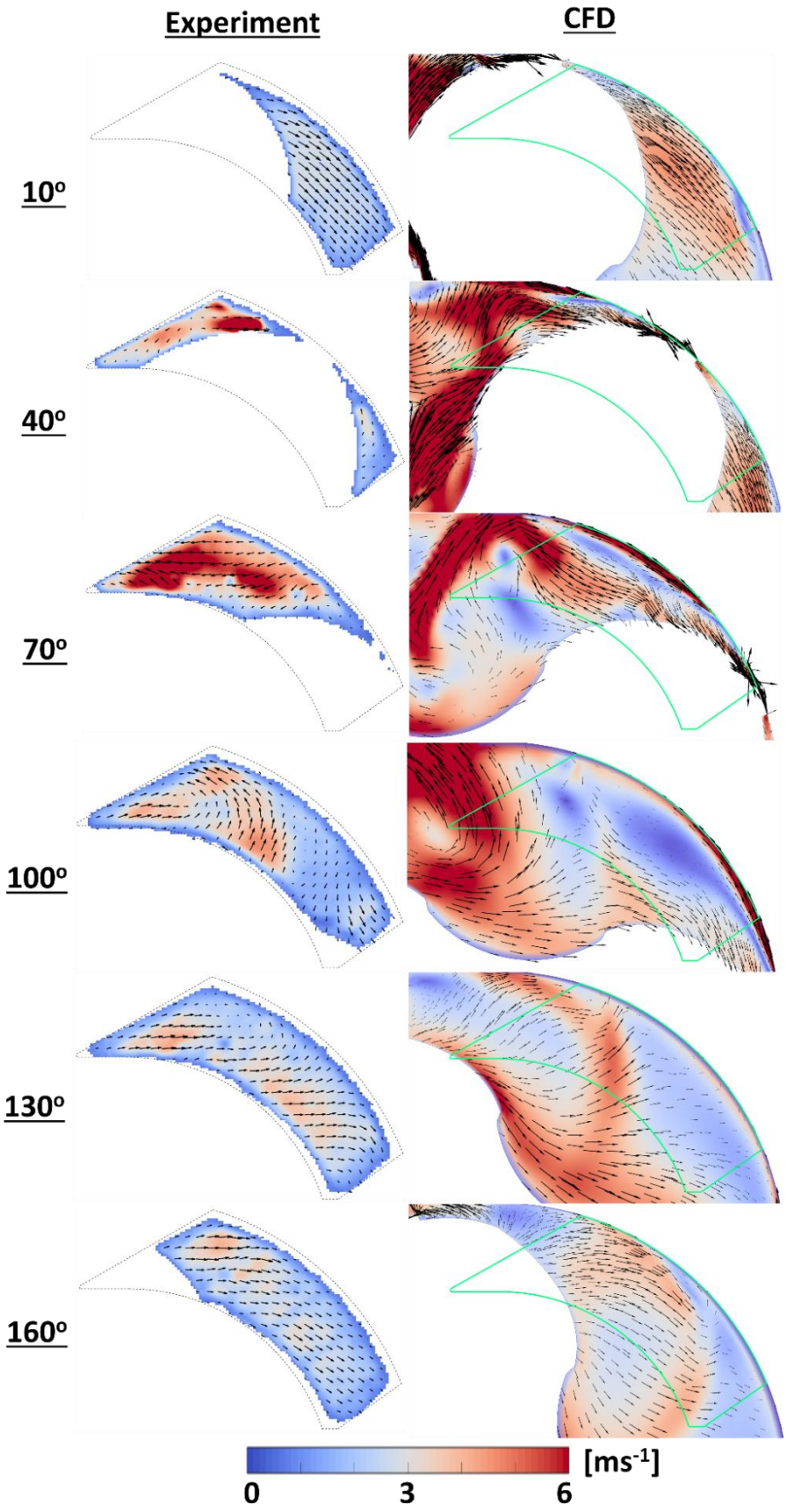

Figure 12. Comparison between the PIV results and CFD results at various crank angle positions and 625rpm rotor speed (Vectors not to scale)

3.3 General flow dynamics inside a Roots blower

The experimental results presented in the previous section could capture only a part of the domain visible through the window whereas the simulation model can provide a detailed view that shows the complete domain and reveal the physical nature of the internal flow. Figure 13 provides a schematic of the three-dimensional unsteady flow field inside a typical two-lobed Roots blower.

This figure is divided into three parts: (i) An isometric view of the Root blower labeled as A. It shows two lobes, inlet at the top and outlet at the bottom, (ii) Side view of the Roots blower, labelled as B, where three-dimensional flow field is depicted above and below the lobes, and (iii) Front view of the Roots blower, labeled as C, showing flow pattern between the Roots blower lobes. A detailed description of these parts is as follows:

(i) Part A provides visualization of the three-dimensional flow field by depicting sample streamlines and vorticity volume rendering inside the Roots blower. Here, streamlines in green color represent low pressure ('L1') and yellow color represents high pressure ('H1' and 'H2') chambers. Visualization of the leakage flows inside the Roots blower domain can be obtained by tracking vorticity magnitude over a given range. This was achieved by generating a volume rendering of the vorticity magnitude between 1500 [s-1] to 25000 [s-1]. Labels 'RL1', 'RL2', 'CV1', 'CV2', 'CV3', etc. shows the presence of the vortices in the domain. The vorticity volume rendering is colored with turbulence kinetic energy, providing a visualization of the mixing caused by the leakage flow. Part A also depicts the position of the cut-planes A and B which reveal various three-dimensional flow structures. (ii) Part B shows a cross-sectional view of plane B by visualizing the tangential velocity vectors which reveal the presence of the twin-vortical flow both above and below the lobe. The leakage is caused by the pressure difference across the rotor lobe, where H1 refers to the high pressure while L1 refers to the low-pressure chambers. The presence of the axial leakage (labeled as 'AL') on the sides can be also be visualized as indicated by large-sized vertical velocity vectors on the sides. (iii) Finally, Part C shows the front-view of the cut-plane A where contours of the flow field relate to the turbulence kinetic energy in the low pressure ('L1') and high pressure ('H1' and 'H2') chambers. The regions of high-mixing are matched with the regions of high leakage flows with 'IL' and 'RL2'. It shows the location of low mixing caused by radial leakages indicated with 'RL1' and 'RL3'.

Figure 13 reveals the three-dimensional nature of the flow-field within a Roots blower where several vortices are generated in the flow chambers with each cycle of rotation. The leakage flow can be divided into axial ('AL'), radial ('RL') and interlobe ('IL) leakages. It is shown that radial leakages ('RL1' and 'RL2') have a marginal effect on turbulent mixing, most likely due to the tight clearances and unique shape provided by the tip stem on each lobe. The radial leakage can suddenly increase when an opening of the flow chamber allows the flow from the high-pressure port to move towards the incoming chamber ('H2'). The H1 chamber quickly assumes the high pressure at the expense of the increased turbulent mixing as shown by radial leakage 'RL2'. The interlobe leakage ('IL') also shows the high mixing region which is expected given challenges to retain tight clearance with the unique tip shape.

Out of the three clearance flow shown in Figure 13A, the axial gap flow has the highest influence on the three-dimensional nature of the flow as well as on the turbulent mixing in the flow. It has a large gap size and the exposed area associated with the axial leakage for Roots blower, thereby large leakage mass flow passing through the axial gaps (labelled as 'AL') would be observed throughout the two lobes. Since the leakage mass flow is

dependent on the gap area, the axial leakage mass flow is largely dependent on the gap size. However, axial leakage also interacts with the other two leakages and impacts the flow field inside the chambers. Corner vortices ‘CV1’ and ‘CV2’ in Figure 13A form when the axial leakage flow interacts with the radial leakages, while corner vortices ‘CV3’ form due to interactions with the interlobe leakage flow. The effect is similar to the corner vortices formed as a part of the secondary flow near the hub side of a highly loaded turbine blade. The turbulent mixing caused by these vortices is one order of magnitude higher than the mixing caused by the radial leakages.

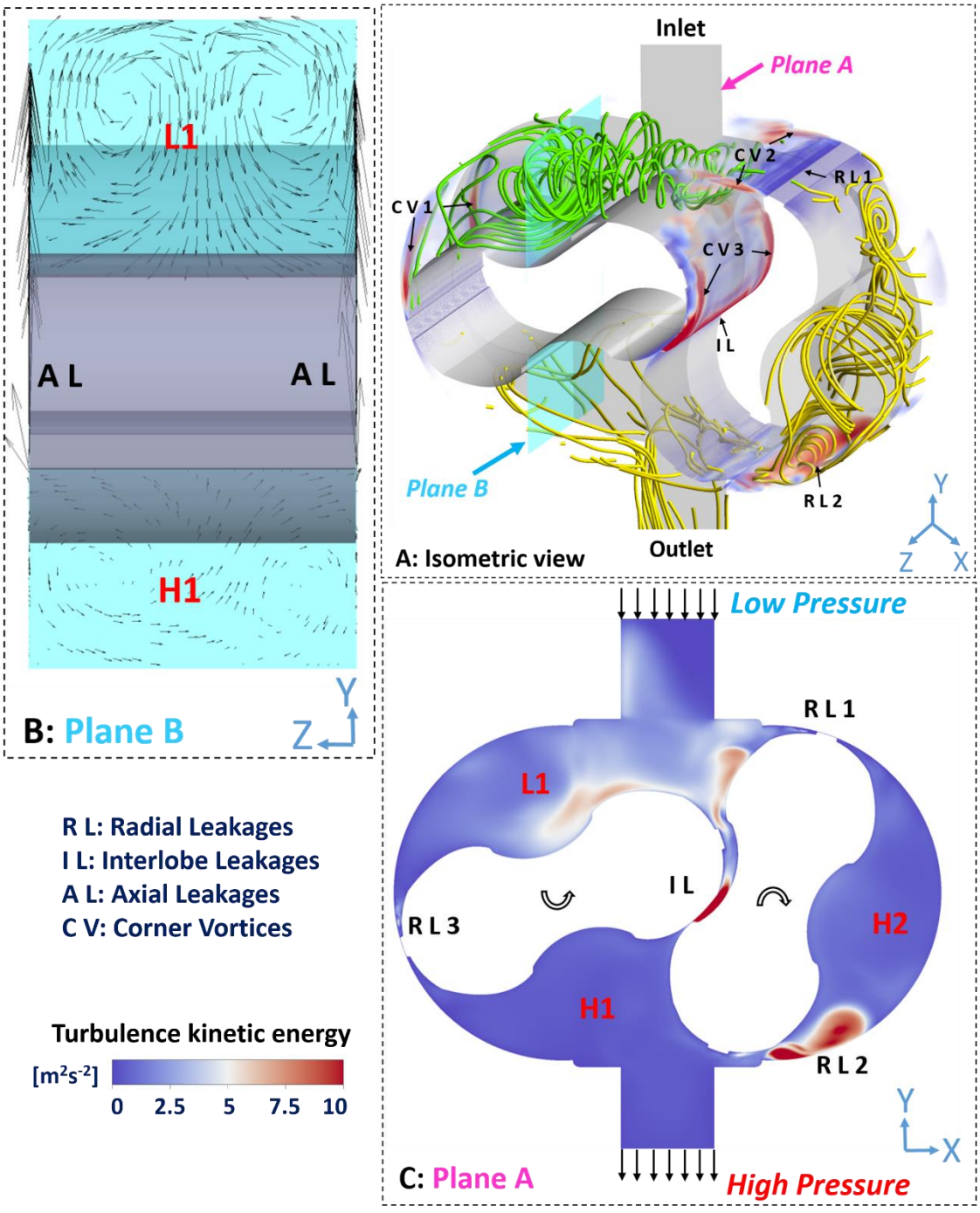

Figure 13. A schematic of three-dimensional unsteady flow field exhibit for a two-lobed Roots blower along with leakage effects

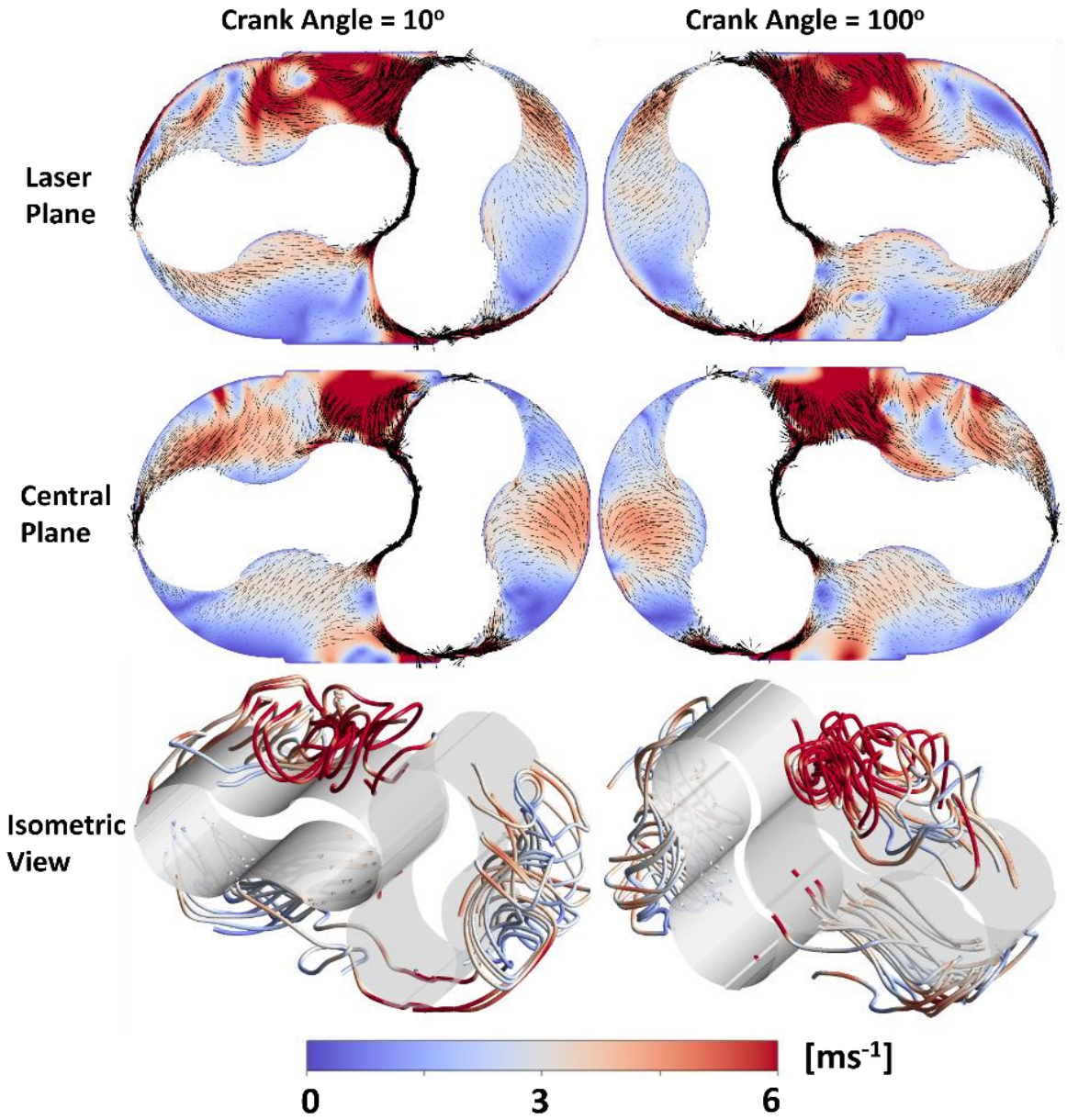

Figure 14. Simulation velocity fields at two different axial planes and crank positions with a 625rpm test case

Much of the flow dynamics elaborated in Figure 13 is expected to remain the same for the majority of positive displacement machines. Axial leakages have the highest impact in terms of turbulent mixing with both radial and interlobe leakages. The second highest impact of the leakage can be derived from the interlobe gap that changes its shape throughout the rotation cycles and experiences maximum fluctuations in the pressure across its ends. Radial leakages have little influence which can be mainly attributed to the tip step geometry which reduces leakage mass flow rate. At times, radial leakages can enhance high mixing when the low-pressure chamber opens towards the high-pressure port. It should be noted that the presence of a tip stem is a design feature specific to the industrial Roots blower employed for this study. It serves the purpose of closing the suction chamber between the lobes earlier and opens later (see Figure 3 for reference). This change in the phase helps in

extending the compression process within the chamber and reduces leakage flow through the radial gap.

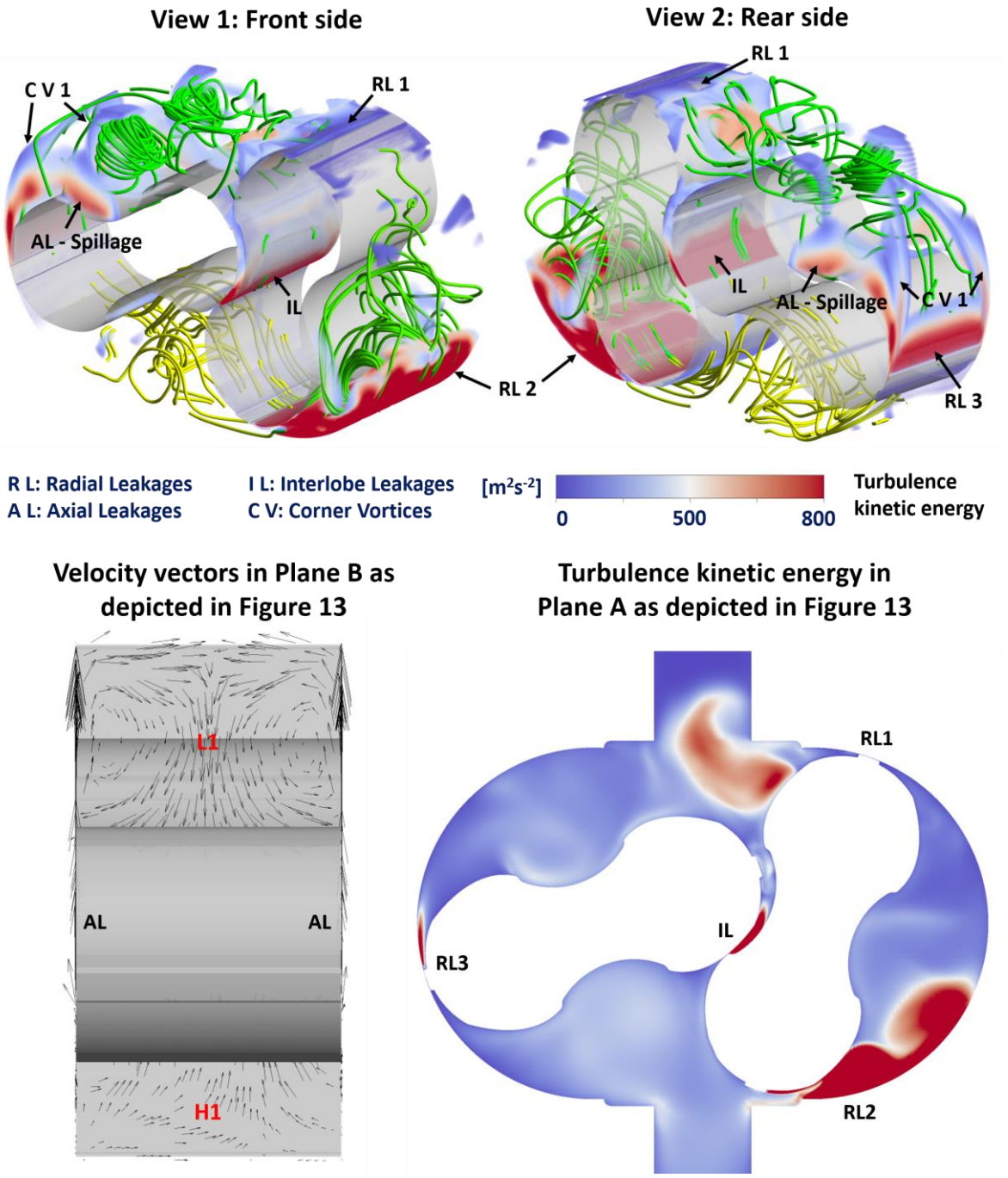

Figure 15. Roots blower flow field at machine design flow conditions

Figure 14 shows the velocity magnitude superimposed by vectors at two different axial planes within the entire rotor domain. In this figure, only plots at 625rpm are provided. The flow fields in the top row are on the laser plane located at a distance of 5mm from the side wall (see Figure 1b). The crank angles are set to 10° and 100°, revealing flow regimes both downstream and upstream of the rotor lobe. The velocity field in the middle row is in the central plane located at the midpoint between the two side walls. The bottom row provides an isometric view of the flow field with streamlines inside the flow domain between rotors.

These streamlines are colored by the velocity magnitude. Figure 14 reveals a high level of three-dimensionality inside the Roots blower. Both velocity magnitude and flow directions are completely different when the laser plane is compared against the central plane. Streamlines show highly three-dimensional flow map which is constantly changing as rotor lobes rotate. Such unsteady nature of the flow also explains the large standard deviation observed in experiments (Figure 9). Minor oscillations in the calculated flow field which could be a consequence of mesh refinement, numerical nature of the turbulence scheme or even initial conditions can have a large impact on the predictions and could cause issues with convergence. In general, the streamlines show that the flow field contains two large counter-rotating vortices that are located above and below the lobes. This explains the vector field visible in plane B in Figure 13. Additionally, large vortices give rise to the small vortices that yield higher mixing of the flow field.

Figure 15 shows the flow field at 10^{o} crank angle using identical CFD set-up but at machine design conditions i.e. at 5275rpm and a pressure ratio of 2.6. The vorticity volume rendering and turbulence kinetic energy colour are prepared in a similar manner as in the isometric view of Figure 13. However, magnitudes are different i.e. the volume rendering of the vorticity between 15000 [s^{-1}] to 25000 [s^{-1}] and the scale of turbulence kinetic energy values are set between 0 [m^2s^{-2}] to 800 [m^2s^{-2}]. Figure 15 also shows the streamlines within the rotor domain, indicating a highly three-dimensional flow field. The colour of these streamlines relates to the static pressure where green lines refer to the lower pressure while yellow lines refer to the higher pressure. The lower part of the figure contains velocity vector field and turbulence kinetic energy in plane B and plane A, respectively prepared in a similar manner as in Figure 13. Comparing Figure 15 with Figure 13, the general flow features remain the same between the design speed of 5375 rpm and the low-speed of 464 rpm. Similar to the low-speed case, the same pattern for radial, interlobe and axial leakages are observed along with the three-dimensional flow field generated due to these leakages. Figure 15 also shows that axial leakages form corner vortices (see label ‘CV1’) and spillage (see label ‘AL-spillage’) that contributes to the three-dimensional flow field in the chambers. The only difference between Figure 15 and Figure 13 is in the magnitude of the flow quantities. However, it is not possible to conclude their extent, increase in the strength and contribution towards the overall leakage has been changed significantly or not. Such measures require comparing both CFD and experimental results over the entire revolution cycles of the rotors at multiple measurement planes.

3.4 Discussion on computational analysis

Usually, it is difficult to compare the unsteady PIV results with URANS simulation results because of the nature of the model which adopts the Reynolds stress transport equations to impose the influence of turbulence on the time-average velocity. Some researchers use simulation results of LES (Large Eddy Simulation) to compare with the unsteady PIV results [19, 20]. Despite that, there is an indication that the simulation results presented in this paper agreed well with the experimental results.

In the past, many researchers compared the RANS or URANS simulation results with the time-averaged PIV results. Mortensen *et al*. [21] compared the simulation results of a rotor stator mixer from k-ε, SST k-ω and RSM (Reynolds stress model) with the time-average PIV results and found that simulation results over-predicted the dissipation rate of the TKE (turbulence kinetic energy). They indicated that the realizable *k-ε* model was better than the other two turbulence models. Ryan *et al*. [22] adopted the SST-SAS (Scale adaptive

simulation) turbulence model in the simulation of a sonolator liquid whistle and compared the simulation results with PIV time-averaged results. The simulation velocity agreed well with the experimental one, but the turbulence parameters matched with the experimental one poorly. Kurec *et al*. [23] performed the simulation with standard *k-ω*, SST *k-ω* and SST-SAS turbulence model in a pressure exchange passage and validated the simulated results with PIV results. The comparison showed that the SST-SAS model can provide the best prediction of the three turbulence models, but the simulation results are more turbulent than the PIV time-average results. Both Ryan *et al*. [22] and Kurec *et al*. [23] hinted that the CFD results needed to be averaged with different cycles because the PIV time-averaged results almost removed most of the turbulence features of the unsteady flow.

Therefore, for simulation results presented in this study, CFD time-averaged results of several cycles can be checked to encourage improved in the simulation results. The method is similar to averaging PIV results over 120 cycles. Additional improvements in the predictions can be made by applying an SST-SAS turbulence model for these simulations. Finally, in order to understand the impact of the leakage flows and detailed mixing caused by them, LES simulations for the gap regions can be pursued to give a better understanding of the leakage flow dynamics.

4 Conclusions

The following conclusions can be derived from this study on Roots blower flow analysis:

Three different types of optical velocity measurement methods were performed on the optical Roots blower with transparent windows, namely High-speed Camera (HC), Continuous Particle Image Velocimetry (CPIV), and Instantaneous PIV (IPIV). Tests performed at the speeds of 464rpm and 625rpm, operating at pressure ratios between 1.06-1.07bara, revealed the unsteady flow regime within the flow chamber enclosed between the rotors and the casing. Multiple vortical structures were observed with their intensity increasing with the wakes produced by the moving rotors. HC technique showed three-dimensional nature of these vortical structures.

- Out of the three analysed methods, the IPIV technique is the most suitable to capture the Roots blower flow field. However, it has limitations in resolving flow features in regions near gaps and walls.

- A three-dimensional CFD unsteady simulation model of a Roots blower was established and compared with the IPIV results. The simulated velocity field is similar to the experimental results showing the correct main flow directions. However, the difference in the velocity magnitude and the vortex distribution was observed.

- A highly unsteady nature of the flow and the cycle-to-cycle fluctuations are observed for consecutive rotation cycles. These fluctuations were particularly high for the 40° and 70° crank angle positions showing complete mismatch against the computational results. Increasing the sample size from 120 cycles to a higher value may help in resolving these large cycle-to-cycle fluctuations.

- The CFD results revealed the formation of counter-rotating vortices and several small vortices, predominantly when trailing behind the rotor lobes.

- Leakage flows impact both three-dimensionality and turbulent mixing in a Roots blower. Vortices generated by the axial and interlobe leakage flows cause high mixing in the flow. The axial leakage generates a strong corner vortex on the rotor edges. This

induces highly three-dimensional flow in the trailing low-pressure chambers. It is concluded that unsteady behaviour and accurate numerical methods capable of resolving these flow structures must be an integral part of a CFD method used for the analysis of rotating positive displacement machines.

- Although the experimental set-up limited the maximum permissible temperature and consequently maximum speed and pressure ratio, the CFD analysis was performed at the design speed of 5275rpm and pressure ratio of 2.6 bara. It showed similar flow features arising from the leakage flows at both, design and test speeds. However, the extent and the nature of these leakages at the design conditions needs to be validated by experiments.

Future experimental test campaigns should consider IPIV measurements across multiple planes along the rotor length to resolve three-dimensional flow features. This will lead to better understanding of the unexplored interactions of the main and leakage flows. On the computational side, validation of the flow features using more accurate methods such as LES (Large Eddy Simulation) can be useful to determine accurate propagation of the three-dimensional flow dynamics initiated by the leakage flows.

5 Acknowledgments

The authors would like to thank Howden Compressors for allowing to use and modify one of the Howden Roots Blowers in this experiment. The authors gratefully acknowledge financial support from China Scholarship Council (CSC), China in the grant 201708610001, National Natural Science Foundation of China, China in the grant 51839010 and The Key Research and Development Program of Shaanxi Province, China in the grant 2017ZDXM-GY-081 to allow Shuaihui Sun from China to visit City, University of London for this project. This work is sponsored by BAE System and the Royal Academy of Engineering, United Kingdom (RCSRF1617\4\11), both jointly funding the position of Professor Christoph Bruecker, which is gratefully acknowledged herein. The position of MSc Qianhui Li is supported by the German Research Foundation, Germany in the grant DFG 1494/32-1, which is also gratefully acknowledged. Authors are thankful to Mr. Robert Jaryczewski and Dr. Ivan Zadrazil from Dantec for help in setting and demonstrating their equipment used for the part of this work. Authors are thankful to their colleague, Dr. Mohsen Ghavami for his guidance in setting-up experiments in section 2.

6 Competing interests

All authors declare that they have no conflict of interest.

7 References

[1] Stošić N, Smith I K and Kovačević A 2005 *Screw Compressors: Mathematical Modelling and Performance Calculation* (Berlin: Springer-Verlag)

[2] Kovacevic A 2005 Boundary adaptation in grid generation for CFD analysis of screw compressors *International Journal for Numerical Methods in Engineering* 64 401-26

[3] Kovačević A, Stošić N and Smith I K 2007 *Screw compressors - Three-dimensional computational fluid dynamics and solid-fluid interaction* (Berlin: Springer-Verlag)

[4] Rane S 2015 Grid Generation and CFD analysis of variable Geometry Screw Machines. (London: City, University of London)

[5] Rane S, Kovacevic A 2017 Algebraic generation of single domain computational grid for twin screw machines. P-I.Implementation *Advances in Engineering Software* 107 38-50
[6] Kovacevic A, Rane S 2017 Algebraic generation of single domain computational grid for twin screw machines Part II–Validation *Advances in Engineering Software* 109 31-43
[7] Sachs R 2002 Experimental investigation of Gas flows in screw machines. *Faculty of Mechanical Engineering*, Ph.D. Thesis, University of Dortmund
[8] Guerrato D, Nouri J M, Stosic N, Constantine A, and Smith I K 2007 Flow measurements in the discharge port of a screw compressor *Proceedings of the Institution of Mechanical Engineers, Part E: Journal of Process Mechanical Engineering* 222 201-10
[9] Kovacevic A, Arjeneh M, Rane S, Stosic N and Gavaises M 2014 Flow Visualization at Suction of a Twin Screw Compressor. In: *International Screw Compressor Conference 2014,* (Dortmund: VDI Verlag Gmbh)
[10] Liu X M, Lu J, Gao R H and Xi G 2013 Numerical Investigation of the Aerodynamic Performance Affected by Spiral Inlet and Outlet in a Positive Displacement Blower *Chinese Journal of Mechanical Engineering* 26 957-66
[11] Liu X M and Lu J 2014 Unsteady Flow Simulations in a Three-lobe Positive Displacement Blower *Chinese Journal of Mechanical Engineering* 27 575-83
[12] Sun S K, Zhao B, Jia X H, and Peng X Y 2017 Three-dimensional numerical simulation and experimental validation of flows in working chambers and inlet/outlet pockets of Roots pump *Vacuum* 137 195-204
[13] Sun S K, Jia X H, Xing L F and Peng X Y 2018 Numerical study and experimental validation of a Roots blower with backflow design *Engineering Applications of Computational Fluid Mechanics* 12 282-92
[14] Ashish M. Joshi, David I. Blekhman, James D. Felske, John A. Lordi, and C.Mollendorf J 2006 Clearance Analysis and Leakage Flow CFD Model of a Two-Lobe Multi-Recompression Heater *International Journal of Rotating Machinery* 2006 1-10
[15] Sun S H, Kovacevic A, Bruecker C, Leto A, Ghavami G, Rane S and Singh G 2018 Experimental Investigation of the Transient Flow in Roots Blower. In: *24th International Compressor Engineering Conference,* (Chicago: Purdue University)
[16] Raffel M, Willert CE, Wereley ST, Kompenhans J, 'Particle Image Velocimetry – A Practical Guide', 2e, Springer, p86-88
[17] Westerweel J (2000) Theoretical analysis of the measurement precision in particle image velocimetry. Exp Fluids 29: S3–S12
[18] Sun S H, Kovacevic A, Bruecker C, Leto A, Singh G, and Ghavami M; 2018 Numerical and Experimental Analysis of Transient Flow in Roots Blower. In: *10th International Conference on Screw Machines (ICSM2018),* (Dortmund: TU Dortmund University)
[19] Ji B, Luo X W, Arndt R E A, Peng X and Wu Y 2015 Large Eddy Simulation and theoretical investigations of the transient cavitating vortical flow structure around a NACA66 hydrofoil *International Journal of Multiphase Flow* 68 121-34
[20] Liu M, Gao Z, Yu Y, Li Z, Han J, Cai Z, and Huang X 2018 PIV experiment and large eddy simulation of turbulence characteristics in a confined impinging jet reactor *Chinese Journal of Chemical Engineering*

[21] Mortensen H, Arlov D, Innings F and Håkansson A 2018 A validation of commonly used CFD methods applied to rotor-stator mixers using PIV measurements of fluid velocity and turbulence *Chemical Engineering Science* 177 340-53
[22] Ryan D J, Simmons M J H and Baker M R 2017 Determination of the flow field inside a Sonolator liquid whistle using PIV and CFD *Chemical Engineering Science* 163 123-36
[23] Kurec K, Piechna J and Gumowski K 2017 “Investigations on unsteady flow within a stationary passage of a pressure wave exchanger, by means of PIV measurements and CFD calculations” *Appl. Therm. Eng.* 112 610-20
[24] Huang Z F and Liu Z X, “Numerical study of a positive displacement blower”, Proc. IMechE, Vol. 223 Part C: J. Mechanical Engineering Science, 2009. P2309-2316.
[25] Cohen CB, Woollett RR, and Weston KC, “Thermodynamic study of a Roots compressor as a source of high-temperature air”, NACA Technical Note 4025, Lewis Flight Propulsion Laboratory, OH. June 1957.
[26] McDougald, S.; Imrie, B. W.; and Cole, B. N., "An Investigation of the volumetric efficiency of a Roots Blower" (1974). Int Compressor Engineering Conf. Paper 127.
[27] Ucer, S. and Celik, I., "Analysis of Flow-Through Roots Blower Systems" (1980). International Compressor Engineering Conference. Paper 319.
[28] Casari, N; Pinelli, M; Suman, A; Kovacevic, A; Rane, Sham R; and Z, Davide, "Full 3D numerical analysis of a roots blower with open-source software" (2018). *International Compressor Engineering Conference.* Paper 2620
[29] Yi-Bin Li, Dong-Sheng Guo & Xiao-Bin Li (2018) “Mitigation of radial exciting force of rotary lobe pump by gradually varied gap”, Engineering Applications of Computational Fluid Mechanics, 12:1, 711-723
[30] Xing, Linfen; He, Yongning; Wen, Jie; and Peng, Xueyuan, "Three-dimensional CFD Modelling of a Roots Blower for Hydrogen Recirculation in Fuel Cell System" (2018). International Compressor Engineering Conference. Paper 2562
[31] Siddiqui MS and Prasad M, “Flow analysis of positive displacement pump lobe rotor using Ansys Workbench”, International Journal of Professional Engineering Studies, Volume VIII /Issue 5 / Aug 2017
[32] Tong SH and Yang D. C. H., “Rotor Profiles Synthesis for Lobe Pumps With Given Flow Rate Functions”, ASME J of Mechanical Design, Mar-05, Vol. 127, p287-294
[33] Yang D and Tong SH, “The specific flowrate of deviation function based lobe pumps—derivation and analysis”, J of Mechanism and Machine Theory 37 (2002) 1025–1042.
[34] Hsieh, C.F.: “A new curve for application to the rotor profile of rotary lobe pumps.” Mech. Mach. Theory 87, 70-81
[35] Mimmi, G., Pennacchi, P.: “Analytical model of a particular type of positive displacement blower.” IMechE Proc. Part C J. Mech. Eng. Sci. 213(5), 517-526
[36] Wang, P.Y., Fong, Z.H., Fang, H.S.: “Design constraints of five-arc Roots vacuum pumps.” Proc. Inst. Mech. Eng. Part C 216(2), 225-234
[37] Cai, Y., Yao, L., Wei, G.: “Generation of tooth profile for Roots rotor based on virtual linkage associated with Assur group”, J Advances in Mech Eng, 2016, Vol. 8(12) 1–8
[38] Y.H. Kang, H.H. Vu and C.H. Hsu (2012). “Factors Impacting on Performance of Lobe Pumps: A Numerical Evaluation.” Journal of Mechanics, 28, pp 229238
[39] Y.H. Kang, H.H. Vu, “A newly developed rotor profile for lobe pumps: generation and numerical performance assessment”, J. Mech. Sci. Technol. 28 (3) (2014) 915-926
[40] Hsieh, C. F. (2015). Flow characteristics of Roots pumps with multistage designs by CFD investigation. Mechanics & Industry, 16(6), 601(11 pages).

[41] Hsieh, C. F., & Deng, Y. C. (2015). A design method for improving the flow characteristics of a multistage Roots pumps. Vacuum, 121, 217-222.
[42] Voorde JV, Vierendeels J, Dick E, “Flow simulations in rotary volumetric pumps and compressorswith the fictitious domain method.” Journal of Computational and Applied Mathematics. 168 (2004) 491–499.